NANO LETTERS

Letter

pubs.acs.org/NanoLett

On the Nanoengineering of Superhydrophobic and Impalement Resistant Surface Textures below the Freezing Temperature

Tanmoy Maitra, Manish K. Tiwari,* Carlo Antonini, Philippe Schoch, Stefan Jung, Patric Eberle, and Dimos Poulikakos*

Laboratory of Thermodynamics in Emerging Technologies, Department of Mechanical and Process Engineering, ETH Zurich, Zurich 8092, Switzerland

Supporting Information

ABSTRACT: The superhydrophobic behavior of nano- and microtextured surfaces leading to rebound of impacting droplets is of great relevance to nature and technology. It is not clear however, if and under what conditions this behavior is maintained when such surfaces are severely undercooled possibly leading to the formation of frost and icing. Here we elucidate key aspects of this phenomenon and show that the outcome of rebound or impalement on a textured surface is affected by air compression underneath the impacting drop and the time scale allowing this air to escape. Remarkably, drop impalement occurred at identical impact velocities, both at room and at very low temperatures (−30 °C) and featured a ringlike liquid meniscus penetration into the surface texture with an entrapped air bubble in the middle. At low temperatures, the drop contact time and receding dynamics of hierarchical surfaces were profoundly influenced by both an increase in the liquid viscosity due to cooling and a partial meniscus penetration into the texture. For hierarchical surfaces with the same solid fraction in their roughness, minimizing the gap between the asperities (both at micro- and nanoscales) yielded the largest resistance to millimetric drop impalement. The best performing surface impressively showed rebound at −30 °C for drop impact velocity of 2.6 m/s.

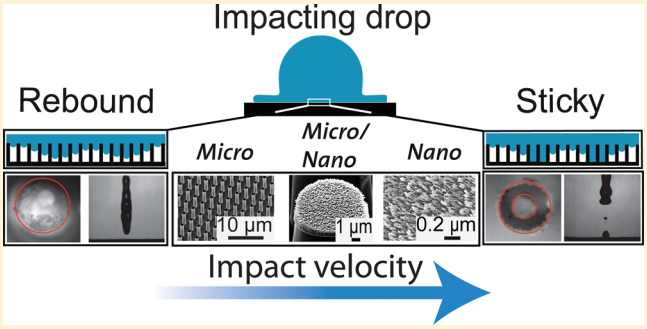

KEYWORDS: *Hierarchical surface morphology, superhydrophobicity, supercooling, anti-icing, drop impact*

Nanotextured surfaces in nature or human-made have been proven to exhibit unique and very valuable properties when it comes to interactions with liquids, ranging from extreme liquid affinity to extreme repellency,[1,2] enhanced thermal transport,[3,4] and ice formation retardation.[5−7] The icing phenomenon in particular can have tremendous natural and technological implications.[8] Infrastructure elements and aircraft industry are severely affected by undesirable icing and are likely to benefit markedly by potential passive, facile, energy saving approaches to mitigate it.[9−11] Use of hydrophobic textured surfaces for anti-icing is motivated by the high water repellency of these surfaces. Through research on both natural[12] and artificially fabricated surfaces,[13] it has now been well established that the presence of a hierarchical morphology and low surface energy materials are key elements needed to prepare solid surfaces with extreme liquid repellency and low liquid adhesion. At static conditions, a surface displaying liquid droplet receding contact angle of over 135°[14,15] and contact angle hysteresis (difference between the advancing and the receding contact angles) lower than 10° is considered to be superphobic to the given liquid.[1,13,16,17] Superhydrophobic surfaces have also been analyzed for anti-icing applications. However, texturing, which is inherently linked to superhydrophobicity, if imposed without accounting for nucleation thermodynamics, can reduce the energy barrier for heterogeneous nucleation. As a result, while some studies have reported significant delay in droplet freezing on superhydrophobic surfaces,[18,19] others have noted the critical importance of roughness control.[11,20]

Given the success of textured surfaces with respect to liquid repellency in static conditions, even for low surface tension liquids,[21,22] these surfaces have also been extensively analyzed[23−28] for their ability to resist dynamically impacting liquid droplets at room temperature. Some studies of droplet impact in cold conditions have also been reported.[6,29,30] The major interest in using textured hydrophobic surfaces at low surface temperatures lies in the fact that an impacting droplet can avoid getting impaled in to the texture and bounce off after impact, thereby avoiding freezing. Mishchenko et al.[6] performed droplet impact tests on microstructured surfaces down to −25 to −30 °C and used droplet temperatures in the range of −5 to 60 °C. Using room temperature droplets, Alizadeh and co-workers investigated droplet impact on surfaces down to −25 °C.[29,30] Despite progress, the

Received: October 4, 2013
Revised: November 25, 2013
Published: December 9, 2013

   dx.doi.org/10.1021/nl4037092 | *Nano Lett.* 2014, 14, 172−182

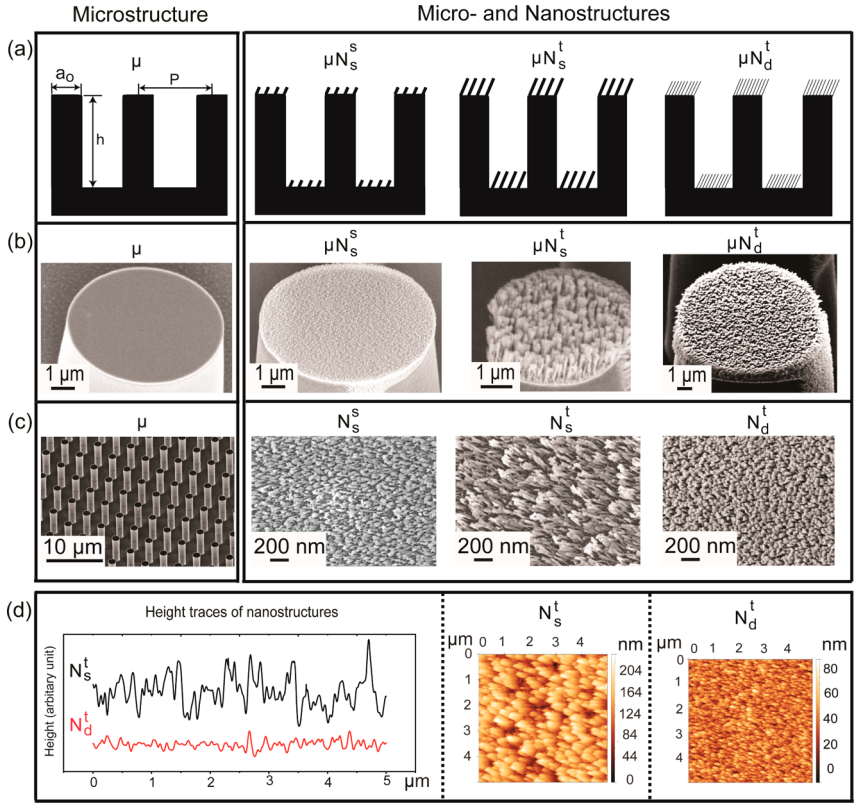

Figure 1. Scheme of fabricated surfaces with controlled micro, nano and hierarchical morphology. (a) Schematics showing the micro and hierarchical morphologies. (b) SEM images of the top of the micropillars. (c) Leftmost panel shows a micropillar array and the remaining three panels show SEM images of nanostructures on top of the micropillars. Three different nanostructures consisting of titanium nanowires: sparse-short, sparse-tall, dense-tall. (d) Two right images show AFM images of the tall nanostructures with two different spacing between the nanowires. The leftmost panel shows the line profiles obtained from the AFM scans to distinguish the nanowire gaps for two nanostructures. For both cases, the AFM tip cannot penetrate the full wire depth, therefore the height profiles in the left image are shown in arbitrary units just to clarify the lateral spacing.

mechanisms (and related criteria) for droplet bounce off or stickiness (penetration and impalement) on textured surfaces, especially at low temperatures, are not well understood. In fact, a systematic control of both micro- and nanostructures comprising hierarchical morphologies is needed to understand the physics of the role of roughness on possible droplet rebound, penetration, or impalement at low temperatures. The goal of the current work is to explore and understand the mechanisms of droplet rebound/impalement of textured surfaces with excellent droplet impalement resistance (water-proofing) properties down to −30 °C. The drop impacts were characterized by dimensionless Weber number (We) defined as $\rho_l V^2 D_0/\gamma$, where the ρ_l denotes the density of the liquid, γ is its surface tension, and the V and D_0, respectively, are the drop velocity and diameter. Our results establish that dynamics of meniscus penetration in the We range $\sim 10^2-10^3$ or lower is controlled by compressibility of air between the impacting drop and the substrate[30,31] and not by the water hammer effect,[26,31] which originates from liquid compressibility.

Results and Discussion. *Morphology Control and Wettability Characterization.* To evaluate the dynamic drop impalement resistance of the textured superhydrophobic surfaces, it was necessary to prepare substrates with controlled morphology. Figure 1 shows a scheme capturing the series of micro-, nano-, and hierarchically textured substrates prepared for this study. Figure 1 also shows the representative morphology of different textures obtained using scanning electron microscope (SEM) and atomic force microscope (AFM). The microstructured surfaces, consisting of circular micropillars in a square array, are designated by the symbol μ. To specify the microstructure in the subsequent discussion, the symbol will be embellished as $\mu^{p}_{a_0}$, where a_0 denotes the diameter of the micropillar and p is the pitch of the square array, both expressed in micrometers (see Figure 1a, leftmost panel). Three different kinds of nanostructures were formed using the glancing angle deposition of titanium (see Materials), which results in the formation of nanowires. The thickness of the deposited titanium film was changed (100 or 400 nm) to alter the nanowire height. The two resulting nanowire heights are referred as short or tall. The angle of deposition was either 80 or 85° to change the density of nanowires in the nanostructures. The resulting density was characterized as dense and sparse, respectively. Thus the nanostructures are designated as N^y_x, where x can be s (sparse) or d (dense) and y can be s (short) or t (tall). Overall, these results in nanostructures referred as sparse-short (short nanowires with a higher gap in between), sparse-tall and dense-tall. Post fabrication, all surfaces were functionalized using 1H,1H,2H,2H-perfluorodecyltrichlorosilane (FDTS) to lower their surface energy and impart hydrophobicity.

Figure 2 shows the result of water droplet contact angle measurement on typical surfaces used in this work. Although we tested a variety of different micro-, nano-, and hierarchical structures, only a few surfaces with an interpillar gap of 2 and 4 μm are shown in Figure 2.

dx.doi.org/10.1021/nl4037092 | Nano Lett. 2014, 14, 172−182

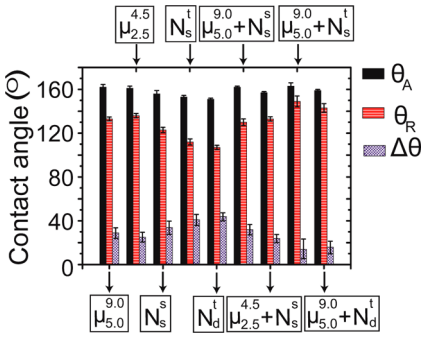

Figure 2. Advancing (θ_A) and receding (θ_R) contact angles and contact angle hysteresis ($\Delta\theta$) on the different micro, nano, and hierarchically textured surfaces.

Contact angles on additional tested surfaces are presented in Supporting Information Figure S1 of Supplementary Section I for brevity. To ensure reproducibility, each measurement in this work was performed at least three times on substrates from at least two different fabrication batches. Therefore, for each data point the shown error bars denote variations over six different measurements. In Figure 2, we have focused on two specific microstructures with small interpillar spacing in order to maximize their expected dynamic droplet impalement resistance,[23] as will be discussed in a more detail below. On any textured hydrophobic surface, minimizing the contact between droplet and solid enhances hydrophobicity. This is typically achieved by minimizing the solid fraction of the textured hydrophobic surface (when viewed from top), aiming at having sessile droplets essentially sitting on air (Fakir state[1]). The solid fraction for a square micropillar array (see Supporting Information Figure S2) can be expressed as

$$\phi = \frac{\pi a_0^2}{4p^2} \tag{1}$$

For both $\mu_{2.5}^{4.5}$ and $\mu_{5.0}^{9.0}$, the solid fraction is $\phi = 0.24$. Because these two surfaces consist of FDTS functionalized Si micropillars, the nearly identical values of both their advancing (θ_A) as well as receding (θ_R) contact angles indicate that the droplet is in Fakir state on these surfaces. This can be understood by employing Cassie equation for θ_A, which assumes that droplet touches only top of pillars, and can be expressed as

$$\cos\theta_A = -1 + \phi(1 + \cos\theta_A^*) \tag{2}$$

where θ_A^* denotes Young's contact angle on the corresponding smooth functionalized Si, which was measured to be 117° ± 2°. Smooth surface here refers to the original silicon wafer functionalized with FDTS on which the average roughness (R_a, obtained from AFM scans) was below 1 nm. The θ_A values on the three tested nanotextured surfaces are very close, thereby indicating that they must have similar solid fraction. Employing θ_A^* on a smooth functionalized titanium surface (R_a below 2 nm), measured to be 115° ± 0.5°, eq 2 and the θ_A measurements in Figure 2, ϕ_N is calculated as 0.19 ± 0.03, 0.22 ± 0.02, and 0.16 ± 0.05, respectively on N_s^t, N_d^t, and N_s^s. Clearly, these solid fraction values are close to each other with their average being 0.19 ± 0.05, although as we see from the Figure 1 the nanowires in the sparse and dense configurations have very different spacing. Thus it is evident that in the sparse case the average diameter of the nanowires should be more than in the dense case in order to have same ϕ_N (see Supporting Information Section II and Supporting Information Figure S3 for a detailed discussion and assessment of ϕ_N for the nanostructures from their SEM morphology images). For hierarchical surfaces, ϕ_H is the product of its values for the micro and nanostructures, that is

$$\phi_H = \phi_\mu \phi_N \tag{3}$$

where the subscripts are used to specify the texture. Since ϕ_μ = 0.24 and ϕ_N values are very close to each other, ϕ_H values for all the hierarchical surfaces shown in Figure 2 should be nearly similar. This explains the nearly identical contact angle measured for all the hierarchical surfaces shown. Furthermore, the very low value of ϕ_H (<0.05) supports the relatively lower contact angle hysteresis for these surfaces, which is under 30° in all measurements on our different substrates.

Influence of Substrate Temperature on Drop Rebound. The influence of substrate morphology on dynamic droplet impalement resistance in cold conditions was evaluated next. The contact time of the droplet on substrate during the impact event is a critical parameter in determining the droplet impalement resistance in cold conditions. Figure 3 shows

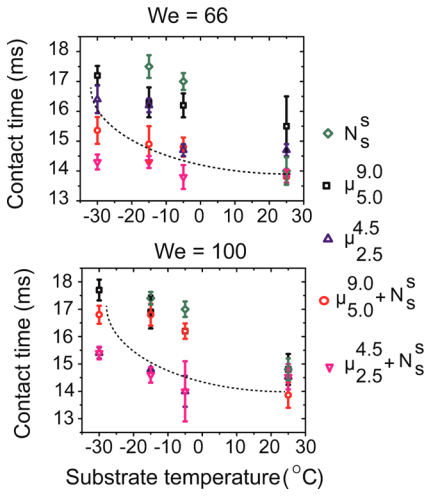

Figure 3. Influence of substrate temperature and morphology on the contact time of the impacting droplets at impact Weber numbers of ~66 and ~100. The contact time is increasing with decrease in substrate temperature due to a steep rise in water viscosity. Note that at high undercooling (−30 °C) the contact time for two surfaces with identical solid fraction, for example, two microstructured substrates having ϕ_μ = 0.24, is different at We ~ 100. The reason is explained in the text. The blue dotted line in the top and bottom plots is simply a guide to the eye. The contact time is not shown for nanotextured surface at −30 °C since the droplet did not rebound in this case.

plots of contact time on different substrates as a function of substrate temperature. The droplets were produced at standard room conditions (temperature 23 °C, humidity 25−40%). The results are shown for two values of We. Some immediate observations can be made from Figure 3. First, it is clear that for all the substrates, the contact time increases with decrease in substrate temperature, as clarified by the dotted blue line, which was added simply as guide to the eye.

Second, although at room temperature the contact time values for different substrates overlap within experimental errors, at lower temperatures the contact time is lower on hierarchical substrates compared to the other textures. Third, on the nanotextured surface, the droplet failed to rebound at

dx.doi.org/10.1021/nl4037092 | Nano Lett. 2014, 14, 172−182

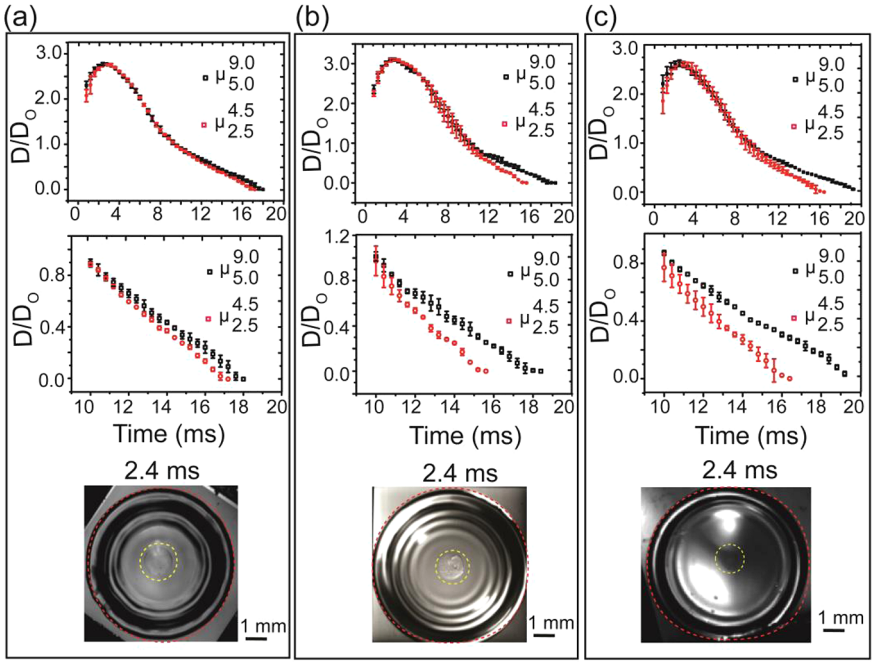

Figure 4. Evolution of normalized droplet-substrate contact diameter on the microstructured surfaces $\mu_{2.5}^{4.5}$ and $\mu_{5.0}^{9.0}$ (having same ϕ). Before impact, the droplets were at room temperature. (a) Water droplet impact at We ~66 on substrates at ~−30 °C. (b) Water droplet impact at We ~100 on substrates at ~−30 °C. (c) Impact of water and glycerin mixture (50/50 by weight) droplet at We ~100 on substrates at room temperature. The second row of images captures the diameter evolution in the late slow stage of droplet recoiling. The top view snapshots shown in the third row show the maximum spreading diameter (marked by the red dashed circle) and the yellow dashed circle indicates a local change in droplet solid interface that seems to impale into the surface texture. Clearly the late stage dynamics is significantly different on the two substrates in the high We cases in (b) and (c). This must be related to the different contact time measured on these surfaces at low temperature.

substrate temperatures below −15 °C. Remarkably, on our hierarchical substrate $\mu_{2.5}^{4.5} + N_s^s$, droplets completely rebounded at the substrate temperature of −30 °C. The physics of the droplet contact time on substrate temperature and texture can be understood by invoking the effects of rise in liquid viscosity with decrease in temperature and, quite crucially, by deciphering the dependence of partial penetration of liquid meniscus in to the texture on impact speed (We). We discuss these two effects consecutively in the sequel.

Immediately upon contact the droplet temperature starts to decrease. Within the time scale of droplet impact τ_{im} ~15 ms, we can estimate the thermal penetration depth[32] to be $\delta_T \sim (\alpha\tau_{im})^{1/2}$ ~45 μm, where a thermal diffusivity of water of 1.3 × 10^{-7} m^2/s was used. Therefore, despite a relatively small level of thermal penetration, use of viscosity increase to explain a rise in viscous dissipation is justified; indeed, the liquid layer nearest to the substrate should experience the maximal viscous shear stress. A reduction in water temperature from room temperature (23 °C) to −27 °C leads to a 5-fold increase in viscosity.[33] This strong viscosity increase explains the increase in the contact time with substrate temperature, since the droplet dissipates more energy through viscous effects both in its interior and through dissipation at the contact line.[33] The dissipation at the contact line[33] is particularly strong for the only nanostructured surfaces, which have higher contact angle hysteresis. This leads to the droplet not rebounding on this surface at low temperature (below −15 °C). The viscosity rise can also explain the relatively lower contact time observed for hierarchical surfaces compared to the corresponding microstructured surfaces, due to the lower solid fraction of the hierarchical surface. As a side note, the presence of air pockets on the microstructured surface have a negligible effect on the heat transfer between the liquid drop and the solid substrate, since the difference of thermal resistance of the silicon pillar-air layer to only silicon layer is insignificant, as explained in the detailed calculation in the Supporting Information (Supplementary Note V).

In addition to the discussion above, there is a very important aspect of the data in Figure 3 that cannot be interpreted merely by considering the solid fraction ϕ and the contact angle hysteresis difference. Figure 3 shows a clear difference in the contact time for two microstructures at low temperature, even though they have the same ϕ. The effect is particularly apparent in the We ~100 case. A similar difference is also apparent in the corresponding hierarchical structures. We will show that this outcome emerges from a subtle but important physical reason, which will help in developing a deeper understanding of what causes substrate impalement resistance at low temperatures. We need to start with a detailed analysis of the droplet impact dynamics.

Liquid Meniscus Impalement and Viscosity Effect. Figure 4 shows the evolution of droplet contact diameter with time on the substrates $\mu_{2.5}^{4.5}$ and $\mu_{5.0}^{9.0}$. Figure 4a,b shows the diameter evolution at two different We values of 66 and 100 and with substrates maintained at −30 °C. The contact diameter D was normalized with the initial droplet diameter D_0. Supporting Information Video V1 shows droplet impact on $\mu_{2.5}^{4.5}$ surface at We ~100. At both We values, droplets spread into a thin disc form, converting the kinetic energy into surface energy, after which they recoiled to lift off from the substrate. It is clear from Figure 4 that in all cases the recoiling stage lasts longer than the spreading stage and it features two distinct regimes with differing rates of diameter decrease. The transition between these two regimes occurs at ~10 ms, as is clear from the second

dx.doi.org/10.1021/nl4037092 | Nano Lett. 2014, 14, 172−182

row of images in Figure 4, which only show the droplet evolution toward the end of the receding phase. The difference between the two receding stages lies in the fraction of droplet that is already off from the substrate. In the slower (late) receding stage, the droplet is almost completely elongated into a cylinder and just about to take off from the substrate. This elongated phase should require a relatively larger fraction of total droplet energy into surface energy, thus explaining the droplet slow down. Although the slowdown appears for both substrates and at both the We numbers, interestingly the late stage diameter evolution rate for the two substrates are significantly different at the higher We (see the second row image in Figure 4b).

To test if the above difference is only due to the change in water viscosity due to its contact with the substrates at low temperature, we investigated the impact dynamics using droplets of 50/50 (by weight) mixture of water and glycerin, having the same viscosity as water at −27 °C.[33] The result for We ∼100 is shown in Figure 4c. Indeed, the late stage dynamics for the two substrates appears to have similar difference as in the case of water droplet impacting on these substrates at −30 °C. As an aside, we note that the maximum spreading diameter in Figure 4c is lower than that in Figure 4b. This is because during the spreading stage (lasting for only ∼2.4 ms), for a water droplet impacting on cold substrates the thermal penetration depth, and thus, the corresponding rise in viscosity will be small. Therefore, the viscous dissipation in water/glycerin mixture impacting on substrates at room temperature should be higher than that for water droplet impact on the substrates at −30 °C. Note that the decrease in temperature should increase the water surface tension, an effect which is not favorable to the noted D_{max} in these two cases. However, rise in surface tension is small (∼10% in the temperature range tested), therefore unlikely to significantly affect this outcome.

On the basis of the above, the difference in the observed receding dynamics at the late stage cannot be explained solely through the viscosity increase. Since the two microstructures in Figure 4 have identical solid fraction $\phi_\mu = 0.24$ and the viscous dissipation should be dominant at the solid liquid interface, the plausible viscosity-based argument is inadequate. This is also supported by the fact that at the same substrate temperature but lower We the two surfaces show nearly identical dynamics. Therefore, the difference must be related to the increase in We and, more specifically, to a change in droplet solid interface conditions locally in the vicinity of the droplet impact point where the difference appears in the receding stage. To this end, if the meniscus were to partially penetrate into the surface texture, then the resulting area of contact between liquid and solid (i.e., the wetted area) would change. A simple calculation of the wetted area is presented in Supporting Information Note III and plotted in Supporting Information Figure S4. Given the higher density of pillars in the microstructure $\mu^{5.0}_{2.5}$, for the same penetration depth its wetted area is higher that the $\mu^{9.0}_{5.0}$ surface. However, this can be reversed if the meniscus penetration on these surfaces is different (see Supporting Information Figure S4). As we will show in the sequel, such a difference in meniscus penetration is in fact favorable due to the closer proximity of pillars in $\mu^{5.0}_{2.5}$. The closer pillars yield a higher capillary pressure (see eq 4) that helps to resist liquid meniscus penetration. Given the importance and implications of the local variation in the droplet/solid wetted interface and potential meniscus penetration on altering the droplet contact time, we recorded the droplet impact events on our substrates in top view. The lowest row in Figure 4 contains representative top view images for impact on surface $\mu^{9.0}_{5.0}$, exactly at the instant of maximum droplet spreading. All these images clearly show a spot at their center (marked by the yellow dashed line), which indicates a depression of the liquid meniscus into the surface texture. This meniscus penetration must be partial and not extend over the entire height of the micropillars, otherwise we would necessarily see impalement and not a complete bounce off of the droplet. Two aspects of meniscus penetration are noteworthy. First, the partial meniscus penetration comes from a local increase in the pressure near the contact point. Second, since partial meniscus impalement is already present in the droplet spreading stage it must occur very rapidly, right after the droplet impacts on the substrate. Therefore, it should not be influenced by substrate temperature. This is confirmed in Figure 5, where we show the partial impalement region (central bright spot) resulting from water droplet impact on our $\mu^{9.0}_{5.0}$ substrate at −30 and 23 °C (room temperature), which are both of identical size. This feature will be discussed and validated through experiments at different substrate temperatures. A clear repercussion of this striking result is that the critical Weber number, We_c, (a substrate specific parameter, beyond which droplet will stick on the surface due to complete penetration and impalement) does not depend on the substrate temperature in the broad range investigated from 23 °C down to −30 °C. Therefore, the partial meniscus penetration below this We_c only influences the droplet contact time and receding dynamics at low substrate temperatures. This influence is critical because an excessively high contact time will increase the possibility of droplet freezing even during the droplet impact phase.

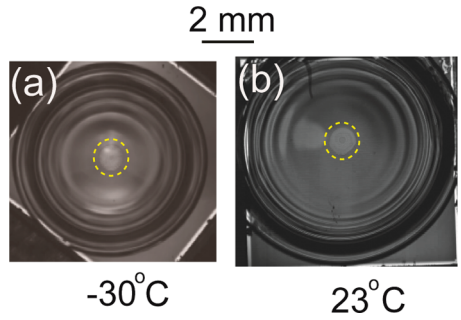

Figure 5. Top view images of droplets at the instant of maximum spreading on $\mu^{9.0}_{5.0}$ substrate at −30 and 23 °C at We ∼ 100. The local meniscus penetration zone near the center is visible in both instances (marked by yellow circle) and is of same size.

The local, ringlike penetration of the liquid meniscus at room temperature has been reported in the literature. Given the obvious similarities in the local, near the droplet impact point, meniscus impalement at room and low substrate temperatures, we analyzed the impalement process with droplet impact experiments at room temperature. The Supporting Information Figure S6 and Supporting Information Videos V2 to V5 capture the important aspects of local meniscus penetration into the texture. From Supporting Information Video V5, the ringlike penetration is apparent. In the Supporting Information Figure S6, the central bright spot (see the zoomed image at 2.4 ms) in the We ∼112 case is an air bubble, which is trapped by the penetrated liquid meniscus. Entrapment of such air bubble has been observed previously.[23,27]

dx.doi.org/10.1021/nl4037092 | Nano Lett. 2014, 14, 172−182

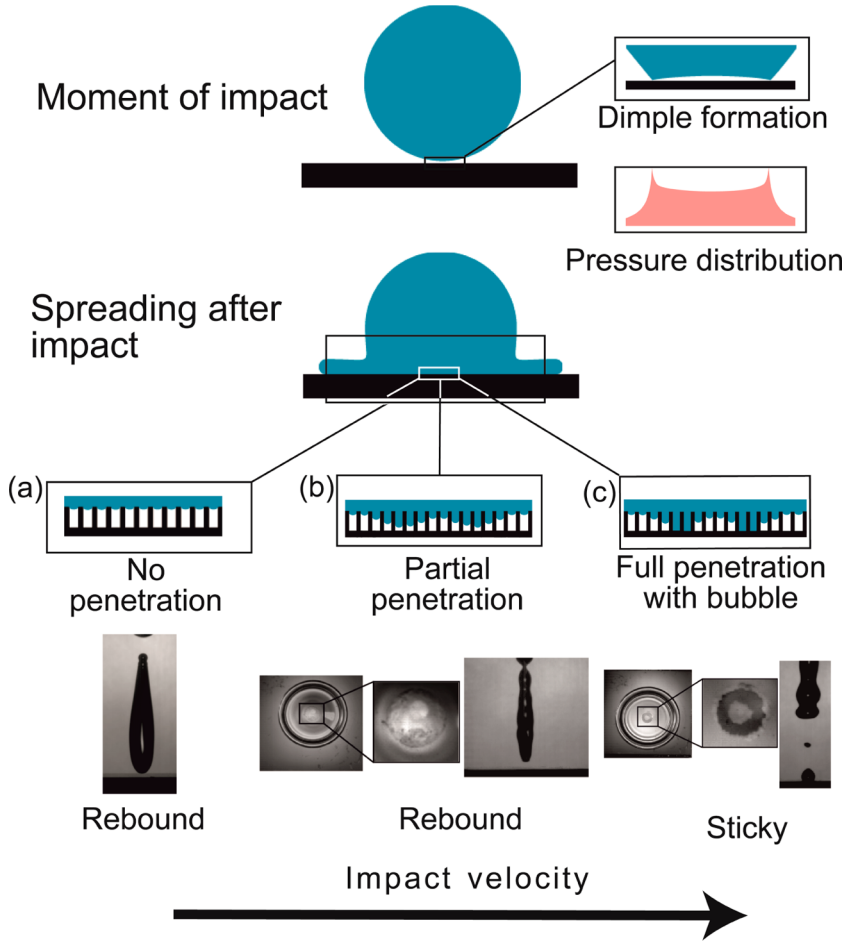

Figure 6. Mechanism of dimple formation and droplet deformation by draining air. The dimple formation and associated rise in pressure near the impact point explain the meniscus penetration. On top the droplet impact, dimple formation and the resulting pressure profiles are shown schematically. Our results indicate that at lower impact velocity (We) the meniscus penetrates partially, whereas beyond a critical velocity the ring like peak in the pressure profile engenders ring like penetration of the meniscus. Schematics in (a−c) show the difference impalement conditions. Below these schematics the high-speed snapshots show the corresponding experimental repercussions. The partial impalement is visible as bright spots top view images shown (the zoom in images are used to highlight them). Above a critical impact velocity, the ring like penetration of the meniscus into the texture is obvious in the top view image under the schematic in (c), which clearly shows a dark impaled ring surrounding a centrally trapped air bubble.

Predictive Model for Meniscus Impalement: Air and Not Liquid Compressibility. In the literature, a pressure balance argument is used to explain the local meniscus transition. Any textured hydrophobic surface should resist penetration of liquid meniscus into it due to its unfavorable wettability condition. This liquid penetration resistance can be quantified through so-called capillary pressure[34]

$$P_C = -\left(\frac{4\phi}{a_o(1-\phi)}\right)\gamma \cos\theta_A^* \tag{4}$$

This resistive pressure must be overcome by pressure generated by the droplet impact process in order to realize penetration of liquid meniscus into the surface texture. Clearly, despite identical ϕ_μ the resistive pressure P_C will be higher on the $\mu_{2.5}^{5.0}$ surface than on the $\mu_{5.0}^{9.0}$ due to its smaller pillar diameter. This will account for the difference in the level of meniscus penetration on two surfaces and explain the related change in the receding dynamics discussed above.

The capillary pressure P_C in eq 4 must be overcome for any meniscus penetration to occur. Because the dynamic pressure, expressed as

$$P_d = 0.5\rho_l V^2 \tag{5}$$

alone is not able to account for the local penetration effect (see Supporting Information Figure S5 and the related discussion in Supporting Information Note IV), typically the concept of water hammer pressure is invoked to explain the preferential penetration of liquid meniscus near the point of droplet impact.[25,26,28,31] The water hammer pressure comes from sudden deceleration of the liquid upon encountering a solid substrate. It is a manifestation of the liquid compressibility and it can be written as

$$P_{WH} = k_{WH}\rho_l CV \tag{6}$$

where k_{WH} is the water hammer pressure coefficient, C is the velocity of sound in water, and V is the droplet impact velocity. Right after impact, the contact line of the droplet is moving faster than sonic speed, thus the impact shock remains pinned to the contact line. Eventually, the contact line slows down and the shock can overtake it. The radial location at which this happens determines the zone of high pressure near the impact point.[35,36] The diameter of this zone can be estimated as[37]

dx.doi.org/10.1021/nl4037092 | Nano Lett. 2014, 14, 172−182

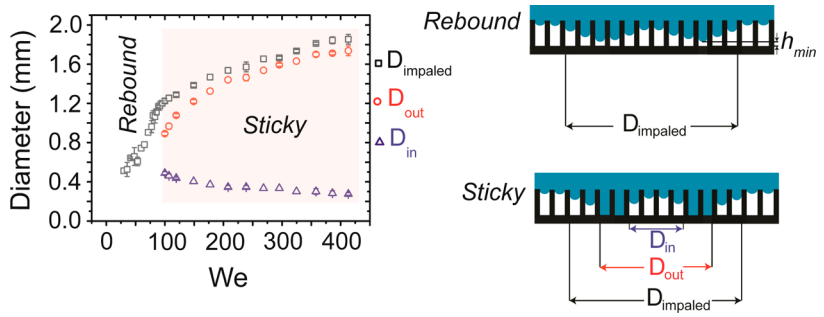

Figure 7. Characteristics of complete rebound to sticky transition during droplet impact on the microstructured substrate $\mu_{5.0}^{9.0}$.

$$d_{WH} = \frac{D_0 V}{C} \tag{7}$$

In the current literature, the maximum reported velocity causing a transition from complete rebound to sticky state was ~8 m/s.[28] This texture-specific threshold velocity for a surface is referred to as its critical velocity, V_c. By using a conservative value of 10 m/s for V_c for our ~2.4 mm diameter droplets, we obtain d_{WH} to be 16 μm. It may also be argued that a more appropriate velocity in the numerator of eq 7 is the spreading velocity after the drop impact, which is larger due to the mass conservation principle. Note that the spreading velocity decreases rapidly after the impact. Thus if we consider the maximum spreading velocity to be ~30 m/s, that is 10 times higher than the impact speed,[38,39] the resulting d_{WH} value comes out to be ~48 μm. This is still considerably smaller that the size of the air bubble appearing during drop impact in our experiments, as can be seen in the Supporting Information Figures S6 and Figure 6 below (bubble diameter ~200 μm or higher). Alternatively, if we consider the time at which pressure release occurs, estimated as $\tau = D_0 V/2C^2 = 8 \times 10^{-10}$ s,[38] and a contact line speed equal to 10 times higher than the impact speed, V, the liquid compressibility effects would affect the meniscus penetration over an area with a characteristic diameter of $d = 10V\tau = 0.024$ μm. However, experiments show that in this area penetration does not occur due to bubble entrapment. Recent works on textured surfaces have pointed out that the water hammer pressure coefficient k_{WH} needs to be reduced by 2 orders of magnitude[26,31] compared to those on smooth surfaces in order to match the experimentally observed critical velocity of transition from rebound to sticky state. Dash et al.[26] proposed to use a balance of the impacting pressures P_{WH} and P_d with the resistive pressure P_c to calculate the coefficient k_{WH}. Their analysis yielded a 2 orders of magnitude lower k_{WH} on a microtextured compared to a flat surface. Furthermore, they suggested that k_{WH} should be a function of P_c. In fact, a similar analysis of our data (shown in Supporting Information Figure S7) indeed agrees with these general conclusions. The rationale for the reduction of k_{WH} was articulated to be the facile drainage of intervening air between the droplet and the substrate as the droplet approaches the textured surface.[26] However, the air bubble entrapment on the textured surfaces as observed in our experiments and also in other works in literature[23,27] contradicts this explanation. Therefore, the air bubble entrapment and 1 order of magnitude larger size of the local penetration zone compared to that expected from water hammer effect point to a very different physical mechanism for local (near impact point) penetration of the liquid meniscus into the surface texture.

For the impact velocity in range of 1 to 10 m/s, which corresponds to We in the range of ~10^2–10^3, the analysis of droplet impact on surfaces shows that the compressibility of the air layer between approaching droplet and the substrate is a key feature guiding the dynamics.[40,41] The air layer must be drained from underneath the droplet in order for the liquid to reach the substrate. The compressed air drainage between droplet and substrate can slow the droplet down and deform it generating a dimple. The dimple formation coincides with a maximum pressure rise in a ringlike region near the impact point.[40,41] This is shown schematically in the top two rows in Figure 6. The range of 1–10 m/s becomes evident by looking at Figure 3b in Mani et al.,[40] who find this to be range of velocity in which there is time to form dimple due to gas compressibility.

Beyond this range the droplet approach will be too rapid and the air layer should be unable to deform the droplet or form the dimple. Because of the axi-symmetric impact, the two symmetric pressure peaks in the schematic in Figure 6 are the cross section of a ringlike pressure peak. This ringlike pressure peak is strikingly consistent with our observation of ringlike penetration of the liquid meniscus into the substrate. Furthermore, the size of the theoretically calculated dimple region is $L \sim 10^2$ μm, which is consistent with our observation of the size of the local penetration zone. On the basis of the above evidence, the compressibility of the draining air, rather than the water hammer pressure effect in the liquid, explains the meniscus penetration observed in our droplet impact tests.

By analyzing the relevant time scales, it can be shown that air bubble entrapment should be feasible during droplet impact on a textured surface. Our analysis is similar to the analysis of air drainage between two coalescing bubbles.[42] The time scale of droplet deformation (dimple formation) by the draining air can be expressed as[40]

$$\tau_{dim} = \frac{R\mathrm{St}^{2/3}}{V} \tag{8}$$

where R is the droplet radius and the $\mathrm{St} = \mu_g/\rho_l VR$ is the Stokes number with μ_g denoting the air viscosity. For $V = 2$ m/s, we obtain $\tau_{dim} \sim 0.1$ μs. To determine the time scale for air drainage, we must balance the pressure gradient driving the air drainage with the viscous stress resisting it. The air must drain across a horizontal length scale of L (the dimple size). During drainage, the excess pressure in the center of the dimple region must approach the Laplace pressure γ/R in the droplet. Thus, equating the pressure gradient with viscous stress gradient in the draining air film we obtain

$$\frac{1}{L}\frac{\gamma}{R} \sim \mu_g \frac{V_d}{h^2} \tag{9}$$

dx.doi.org/10.1021/nl4037092 | Nano Lett. 2014, 14, 172–182

where V_d denotes the air drainage velocity scale and h is the height of the micropillars, which is assumed to be much larger than the dimple height above the substrate. From eq 9, we can obtain the drainage time scale as

$$\tau_d \sim \frac{L}{V_d} \sim \frac{\mu_g R}{\gamma}\left(\frac{L}{h}\right)^2 \tag{10}$$

Substituting the numerical values we obtain $\tau_d \sim 10$ μs. Therefore, the dimple formation occurs nearly 2 orders of magnitude faster than the air drainage. As a result, the pressure profile obtained on a flat surface should also be applicable in our experiments. Note, however, that drainage time scale is much smaller than the droplet spreading and receding time scales (~15 ms). Thus an air bubble entrapment can only occur if the meniscus undergoes a complete ringlike penetration and traps the bubble in the center (see Figures 6 and 7).

In Figure 7, various diameters characterizing the meniscus penetration in the central part of the droplet are plotted for substrate $\mu_{5.0}^{9.0}$ as a function of the We. At We ~100, a transition from complete rebound to sticky state occurs characterized by a ringlike penetration into the texture (i.e., a local transition from Cassie to Wenzel states). In the figure, $D_{impaled}$ denotes the overall diameter of the central region showing impalement. The ring like region between D_{in} and D_{out} is completely penetrated. The D_{in} denotes the size of the trapped bubble. The region extending from D_{out} to $D_{impaled}$ should have partial impalement. The physical reason for partial impalement at intermediate We values can be understood as follows. Because of the pressure peak, the meniscus penetration into the texture will occur for a maximum of $\tau_d \sim 10$ μs, after which the air must drain out. This is evident from droplet impact recordings in top view, where the central bright spot (penetration zone) is visible almost right from the onset of the droplet spreading regime (note that our time resolution in imaging was 0.4 ms, which corresponds to a video recording of 2500 frames per second). In the very initial stage of spreading, a part of droplet remains above the substrate and obstructs the top view. However, in almost all high We impact cases we observed the impalement spot well before the end of droplet spreading phase. Upon coming in contact with the substrate, the sharpened liquid interface at the edge of the dimple should relax. Therefore, unless the velocity is sufficiently high with a corresponding higher value of pressure peak (see the maximum pressure P_{max} calculations below), the meniscus can stop at an intermediate stage while penetrating into the surface texture. This should lead to the partial impalement state shown schematically in Figures 6 and 7.

Predictive Model for Liquid Impalement. In the last segment of this discussion, we will show how the dimple formation and associated pressure rise can explain the penetration of the meniscus and therefore quantify complete bounce off to sticky transitions on substrates of various morphologies. The analysis will also help explain the beneficial role of appropriately designed hierarchical morphology with respect to achieving complete rebound.

On a flat surface, using the asymptotic self-similar solution of Madre et al.,[43] the strength of the pressure peak during the droplet dimple formation can be expressed as[43]

$$P_{max} = \frac{1.4}{\varepsilon h_{min}^{0.5}} \tag{11}$$

where h_{min} is a parameter denoting the minimum air film thickness observed (see Figure 7) before the surface tension force suppress any further sharpening of the dimple edge and ε is a parameter that qualifies whether the gas should be considered compressible or incompressible. These two quantities can be expressed as

$$h_{min} = \frac{2.54 R \mathrm{St}^{14/9}}{\mathrm{Ca}^{(2/3)}} \tag{12}$$

and

$$\varepsilon = \frac{P_0}{R\mu_g^{-1}V^7\rho_l^{4}{}^{1/3}} \tag{13}$$

where $\mathrm{Ca} = \mu_g V/\gamma$ is the capillary number and P_0 is ambient pressure. By combining eq 11 to eq 13, we obtain

$$P_{max} = 0.88\frac{R\mu_g^{-1}V^7\rho_l^4\mathrm{Ca}^{1/3}}{P_0 R^{1/2}\mathrm{St}^{7/9}} \tag{14}$$

At critical velocity the P_{max} should equal P_c. In Figure 8a, we have plotted P_{max} (using the experimental values of velocity

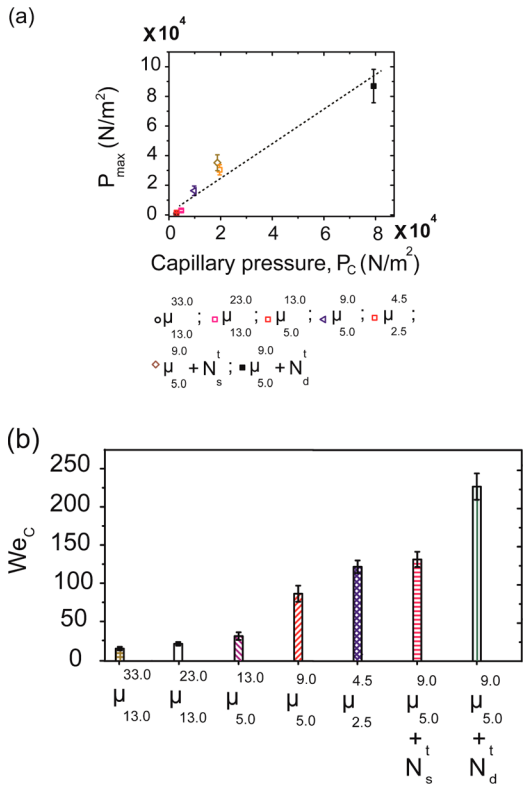

Figure 8. Substrate penetration characteristics in room temperature impact tests. (a) Plot of P_{max} versus P_c for different substrates tested. The slope of the fit line is 1.16, showing validity of argument that dimple formation causes the local penetration of the meniscus at a critical, high impact speed. (b) The corresponding We_c of transition on different microstructured and hierarchical substrates.

corresponding to transition from rebound to sticky state) as a function of P_c for various substrates. For hierarchical surfaces, the solid fraction was obtained using eq 3 and the effective pillar diameter was obtained by employing an ImageJ based image processing of nanotextures obtained from the SEM image of the nanowires. The procedure is described in Supporting Information Section II. The straight line in Figure 8a shows a linear fit. The slope of the line is 1.16. This shows

dx.doi.org/10.1021/nl4037092 | Nano Lett. 2014, 14, 172−182

that P_{max} indeed should be considered as the impalement pressure that causes a local transition from Cassie to Wenzel state (i.e., impalement of the liquid meniscus into the texture). The last data point, for the hierarchical substrate $\mu_{5.0}^{9.0} + N_d^t$ was obtained using droplet of water and isopropanol (IPA) mixture (5% IPA by volume). This is because for that substrate, using water droplet impacts at We ~200 the maximum spreading diameter exceeded our sample size. The water/IPA mixture has lower surface tension[44] (~47.83 mN/m) and contact angle, which result in rebound to sticky transition at a lower critical impact speed. The critical speed so obtained was rescaled using the balance of P_c and P_{max} in order to obtain the critical impact speed for water (see the last paragraph of Supporting Information Note IV for more details). Figure 8b plots the critical Weber number We_c in order to express the role hierarchical morphology on impact resistance. The two microstructures with identical solid fraction but different P_c are also shown.

We must note here that the P_{max} calculated using eq 14 is, strictly speaking, valid for a case of 2D droplet impact on a smooth surface.[40] On textured surfaces, detailed numerical simulations have indeed shown change in the pressure profile.[41] Therefore, the balance of P_{max} and P_c as performed here should be taken as an overall scaling analysis. However, a slope equal to 1.16 is a strong indicator of the validity of this analysis. From Figure 8 it is clear that for the same solid fraction a surface with smaller gap in the asperities is better for dynamic impalement resistance. This is obviously the case for microtextured surfaces $\mu_{5.0}^{9.0}$ and $\mu_{2.5}^{4.5}$. It is also true for the two hierarchical surfaces ($\mu_{5.0}^{9.0} + N_s^t$ and $\mu_{5.0}^{9.0} + N_d^t$) with same microstructure (ϕ_μ) decorated with two nanostructures with same solid fraction (ϕ_N) but different gap between the nanowires. Thus for any given solid fraction, reducing the gap between asperities both at micro and nanoscale is beneficial for impalement resistance.

Meniscus Impalement on Hierarchical Structures. Figure 9 shows the result of droplet impact on substrates at −30 °C in order to establish the fact that for textured surfaces with low pillar gap (i.e., with high dynamic impalement resistance), the We_c determined from room temperature experiments provide excellent guide to the low-temperature impalement resistance. This is because, as argued above, the meniscus penetration time scale is very short since it should be close to the time scale of dimple formation τ_{dim} ~0.1 μs. Therefore, there should be negligible cooling during the penetration and the impalement process and thus should not be affected by the substrate temperature. This is validated in Figure 9, which shows the outcome of impact experiments. We ~120 is beyond the We_c of the microstructured surface $\mu_{5.0}^{9.0}$ at room temperature. In agreement to that, the low-temperature impact also shows a remnant droplet after impact, that is, a sticky behavior. Similarly, on the first hierarchical surface $\mu_{5.0}^{9.0} + N_s^t$ the transition is seen only in We ~140 case and complete rebound is observed at We ~120. The room temperature We_c for this surface (see Figure 8) was ~133. Finally, continuing the trend the $\mu_{5.0}^{9.0} + N_d^t$ surface shows complete rebound at both the We numbers. In fact, the surface showed complete drop rebound up to We of 227 (corresponding to a drop velocity of 2.6 m/s) at ~−30 °C.

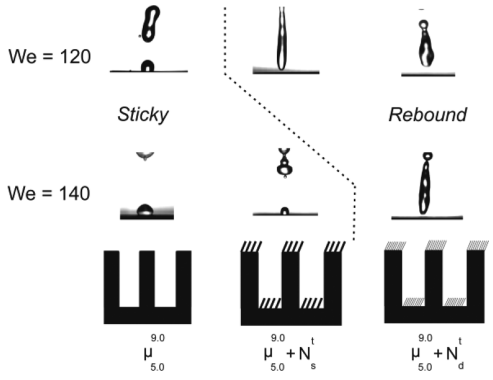

Figure 9. Beneficial role of hierarchical morphology in determining the impact resistance at substrate temperature of −30 °C.

Although the penetration itself is not affected by substrate temperature, it does influence the droplet rebound off the surface. This is because during the receding stage, by the time the receding contact line reaches the central penetration zone the penetrated (whether partially or fully) liquid will have enough time to cool down, thereby making it difficult for the droplet to rebound due to increased liquid viscosity. For the partial impalement regime, the droplet is able to spend part of its initial kinetic energy to pull the meniscus out. However, this must cost additional energy and explains the relatively larger contact time observed for cases with partial impalement in Figure 3b. Upon complete ring like penetration beyond We_c the required energy penalty is too high for the meniscus to be withdrawn, thereby leading to impalement.

Conclusion. The role of morphology of superhydrophobic surfaces, both at micro and nanoscales, in deciding the droplet impalement resistance under severely undercooled conditions was investigated by impacting room temperature droplets on undercooled substrates with precisely designed textures. It was shown that the phenomenon of meniscus impalement in the surface texture is governed by the compressibility of air, and its drainage time scale, from underneath the impacting drop. In this context, we could correctly predict the morphology-dependent We_c for transition from drop rebound to impalement. Interestingly, We_c was independent of substrate temperature in the range from room temperature down to −30 °C due to the fact that meniscus penetration occurred very rapidly at the beginning of the impact, much faster than the heat transfer time scale. Below We_c, the meniscus penetration was partial and it could be retracted from the texture by the receding droplet, thereby rendering complete rebound possible. However, the partial penetration significantly altered the droplet receding dynamics and the contact time on the substrates at low temperatures with associated increase in the liquid viscosity. A hierarchical superhydrophobic surface with minimal spacing between the asperities, both at the micro- and nanoscales, was found to yield best impalement resistance among surfaces with the same solid fraction. Such a surface resisted droplet penetration at We of 227 (corresponding to a drop velocity of 2.6 m/s) even at a substrate temperature of ~−30 °C.

Materials and Methods. *Materials.* Boron doped p-type (100) silicon wafer with resistivity of 0.005−0.2 ohm-cm and thickness of 500 ± 25 μm was used as substrate. Acetone, isopropyl alcohol, *n*-hexane, glycerol and 40% hydrofluoric acid were from Sigma Aldrich. 1H,1H,2H,2H-Perfluorodecyltrichlorosilane (FDTS) $C_{10}H_4Cl_3F_{17}Si$ was purchased from Alfa Aesar. The chemicals were used as received. The deionized (DI) water (18.2 MΩ, Mill-Q pore) was used for contact angle measurements and droplet impact experiments.

Fabrication of Microstructured Surface. The micropillar substrates were 8 × 8 mm in size. To start with, a 500 nm thick

dx.doi.org/10.1021/nl4037092 | Nano Lett. 2014, 14, 172−182

SiO_2 layer was deposited on standard p-doped silicon wafer by plasma enhanced vapor deposition process (PECVD). Thereafter, the SiO_2 deposited silicon wafer was photolithographically patterned using a Karl Suss MA6 mask aligner and Shipley S1813 positive photoresist. The pattern was then transferred on to the SiO_2 layer by reactive ion etching[45] process employing CHF3/Ar plasma. The patterned SiO_2 layer was used as hard mask for subsequent silicon etching process. Following pattern transfer on the SiO_2 layer, the photoresist was removed using by acetone. The wafer was then diced into 8 × 8 mm size chips. To transfer the pattern into silicon, silicon cryo-etching process was followed in an inductive coupling plasma reactor (Oxford Instruments, ICP 180) using SF_6/O_2 plasma at −100 °C. After the silicon etching, the SiO_2 hard mask was removed by treating with 1:5 diluted 40% HF solution.

Fabrication of Nanostructures. For nanostructures, titanium metal was evaporated on the microstructures or on smooth surfaces using the glancing angle deposition technique[46] in an electron beam assisted physical vapor deposition system. In this technique, substrates are held at an angle with respect to the source. The angular configuration facilitates metal deposition in the form of nanowires rather than uniform film. By varying the angle and amount of deposited material, three different nanostructures N_d^t, N_s^t, and N_s^s were fabricated. A substrate angle, called glancing angle, of 85° was used for sparse nanowire structures, and an angle of 80° was used for dense nanowire structure. The height of nanowires was changed by depositing either 100 or 400 nm of film. Simple evaporation was used to form a smooth titanium film required for measuring the Young's contact angle.

Functionalization of Self-Assembled Monolayer. After texturing and cleaning, all fabricated substrates were treated with FDTS $C_{10}H_4Cl_3F_{17}Si$ (96% Alfa Aesar) in *n*-hexane solution to form a self-assembled monolayer (SAM)[47] and lower the surface energy of the substrate, rendering them hydrophobic. A ∼2 min immersion time was used for SAM formation. Finally, the substrates were rinsed consecutively in *n*-hexane and isopropyl alcohol and dried with nitrogen.

Surface Characterization. For surface characterization, scanning electron microscope (Zeiss ULTRA 55) and atomic force microscope (Asylum Research, MFP 3D) were used. The AFM images were obtained by taping mode scans performed using super sharp silicon tip (NANOSENSORS) with 2 nm tip diameter.

For contact angle measurements, an in-house goniometer system was used. The system consisted of a zoom lens (Thorlabs, MVL7000) fitted to a CCD camera. A syringe pump (Harvard Instruments) was employed for altering the volume of the droplet on substrates and thereby enabled the measurement of the advancing and receding contact angles.

Experimental Setup. A double layer, transparent experimental chamber made of Plexiglas was used to perform the droplet impact tests. The intervening space between the two layers was evacuated by a vacuum pump to improve the insulation. To control the temperature inside the chamber, a brass pipe was fitted into the chamber and connected to a cold stream of nitrogen vapor. The nitrogen stream was obtained from a cryogenic cooler (Isotherm KGW TG LKW-H) with temperature control system. A brass platform was used to place the test surfaces in the chamber. A small window at the top of the chamber was used to access the substrates and insert the impacting droplets. Two thermal sensors (Pt-1000 2I 161, IST AG) were used to measure the temperature. One measured the ambient temperature inside the inner chamber and the other was attached to the brass table. This temperature was controlled using the temperature control system and taken to be equal the substrate temperature. A humidity sensor (LinPicco A0545, IST AG) was also mounted to monitor the humidity near to the substrate. In our experiments in a subcooled condition, the humidity remained near 0%.

A high-speed camera (Phantom V9.1) was used to record the droplet impact at a frame rate 2500 frames per second. DI water droplets with a 2.4 mm diameter were generated outside the experimental chamber using a fine needle fitted to a syringe pump (PHD Ultra, Harvard Apparatus).

■ ASSOCIATED CONTENT

Ⓢ Supporting Information

Supporting Information includes characterizations of additional surfaces that are not mentioned in the main paper, characterizations of different nanoscale surfaces, dynamic pressure, and water hammer pressure calculations of different microstructured and hierarchical surfaces. Also included are five videos. This material is available free of charge via the Internet at http://pubs.acs.org.

■ AUTHOR INFORMATION

Corresponding Authors

*E-mail: (D.P.) dpoulikakos@ethz.ch. Phone: +41 44 632 27 38. Fax: +41 44 632 11 76.

*E-mail: (M.K.T.) m.tiwari@ucl.ac.uk. Phone: +44 (0) 20 3108 1056.

Author Contributions

D.P. and M.K.T. conceived the problem and designed research. T.M. performed the experiments and characterization with help from P.S. and C.A. and direct mentoring by M.K.T. P.E. contributed in experimental design and microstructure fabrication. Results, discussion, and theoretical analyses were performed by T.M., M.K.T., C.A., S.J., and D.P. D.P. and M.K.T. guided the work. All authors participated in paper writing and commenting.

■ ACKNOWLEDGMENTS

The partial support for this work from the Swiss National Science Foundation (SNF) grant 200021_135479 is gratefully acknowledged. C.A. acknowledges funding by a Marie Curie Intra-European Fellowship within the 7th European Community Framework Programme (ICE^2, 301174).

■ ABBREVIATIONS

SEM: scanning electron microscope; AFM: atomic force microscope; FDTS: 1H,1H,2H,2H-perfluorodecyltrichlorosilane

■ REFERENCES

(1) Lafuma, A.; Quere, D. *Nat. Mater.* **2003**, *2* (7), 457−460.

(2) Tuteja, A.; Choi, W.; Ma, M. L.; Mabry, J. M.; Mazzella, S. A.; Rutledge, G. C.; McKinley, G. H.; Cohen, R. E. *Science* **2007**, *318* (5856), 1618−1622.

(3) Boreyko, J. B.; Chen, C. H. *Phys. Rev. Lett.* **2009**, *103* (18), 184501.

(4) Torresin, D.; Tiwari, M. K.; Del Col, D.; Poulikakos, D. *Langmuir* **2013**, *29* (2), 840−848.

(5) Jung, S.; Tiwari, M. K.; Doan, N. V.; Poulikakos, D. *Nat. Commun.* **2012**, *3*, 615.

(6) Mishchenko, L.; Hatton, B.; Bahadur, V.; Taylor, J. A.; Krupenkin, T.; Aizenberg, J. *ACS Nano* **2010**, *4* (12), 7699−7707.
(7) Varanasi, K. K.; Deng, T.; Smith, J. D.; Hsu, M.; Bhate, N. *Appl. Phys. Lett.* **2010**, *97*, 23.
(8) Marwitz, J.; Politovich, M.; Bernstein, B.; Ralph, F.; Neiman, P.; Ashenden, R.; Bresch, J. *Bull. Am. Meteorol. Soc.* **1997**, *78* (1), 41−52.
(9) Gent, R. W.; Dart, N. P.; Cansdale, J. T. *Philos. Trans. R. Soc. A* **2000**, *358* (1776), 2873−2911.
(10) Authority, C. A. *Aircraft Icing Handbook*. Safety Education and Publishing Unit: New Zealand, 2000; p 2.
(11) Jung, S.; Dorrestijn, M.; Raps, D.; Das, A.; Megaridis, C. M.; Poulikakos, D. *Langmuir* **2011**, *27* (6), 3059−3066.
(12) Quere, D. Wetting and roughness. *Annu. Rev. Mater. Res.* **2008**, *38*, 71−99.
(13) Li, X. M.; Reinhoudt, D.; Crego-Calama, M. *Chem. Soc. Rev.* **2007**, *36* (8), 1350−1368.
(14) Rioboo, R.; Delattre, B.; Duvivier, D.; Vaillant, A.; De Coninck, J. *Adv. Colloid Interface Sci.* **2012**, *175*, 1−10.
(15) Li, W.; Amirfazli, A. *J. Colloid Interface Sci.* **2005**, *292* (1), 195−201.
(16) Tiwari, M. K.; Bayer, I. S.; Jursich, G. M.; Schutzius, T. M.; Megaridis, C. M. *ACS Appl. Mater. Inter.* **2010**, *2* (4), 1114−1119.
(17) Liu, M. J.; Zheng, Y. M.; Zhai, J.; Jiang, L. *Acc. Chem. Res.* **2010**, *43* (3), 368−377.
(18) Guo, P.; Zheng, Y. M.; Wen, M. X.; Song, C.; Lin, Y. C.; Jiang, L. *Adv. Mater.* **2012**, *24* (19), 2642−2648.
(19) Zhang, Q. L.; He, M.; Chen, J.; Wang, J. J.; Song, Y. L.; Jiang, L. *Chem. Commun.* **2013**, *49* (40), 4516−4518.
(20) Cao, L. L.; Jones, A. K.; Sikka, V. K.; Wu, J. Z.; Gao, D. *Langmuir* **2009**, *25* (21), 12444−12448.
(21) Tuteja, A.; Choi, W.; Mabry, J. M.; McKinley, G. H.; Cohen, R. E. *Proc. Natl. Acad. Sci. U.S.A.* **2008**, *105* (47), 18200−18205.
(22) Kota, A. K.; Li, Y. X.; Mabry, J. M.; Tuteja, A. *Adv. Mater.* **2012**, *24* (43), 5838−5843.
(23) Reyssat, M.; Pepin, A.; Marty, F.; Chen, Y.; Quere, D. *Europhys. Lett.* **2006**, *74* (2), 306−312.
(24) Jung, Y. C.; Bhushan, B. *Langmuir* **2009**, *25* (16), 9208−9218.
(25) Deng, T.; Varanasi, K. K.; Hsu, M.; Bhate, N.; Keimel, C.; Stein, J.; Blohm, M. *Appl. Phys. Lett.* 2009, *94*, (13).
(26) Dash, S.; Alt, M. T.; Garimella, S. V. *Langmuir* **2012**, *28* (25), 9606−9615.
(27) Tsai, P. C.; Hendrix, M. H. W.; Dijkstra, R. R. M.; Shui, L. L.; Lohse, D. *Soft Matter* **2011**, *7* (24), 11325−11333.
(28) McCarthy, M.; Gerasopoulos, K.; Enright, R.; Culver, J. N.; Ghodssi, R.; Wang, E. N. *Appl. Phys. Lett.* **2012**, *100*, 26.
(29) Alizadeh, A.; Yamada, M.; Li, R.; Shang, W.; Otta, S.; Zhong, S.; Ge, L. H.; Dhinojwala, A.; Conway, K. R.; Bahadur, V.; Vinciquerra, A. J.; Stephens, B.; Blohm, M. L. *Langmuir* **2012**, *28* (6), 3180−3186.
(30) Alizadeh, A.; Bahadur, V.; Zhong, S.; Shang, W.; Li, R.; Ruud, J.; Yamada, M.; Ge, L. H.; Dhinojwala, A.; Sohal, M. *Appl. Phys. Lett.* **2012**, *100*, 111601.
(31) Kwon, H. M.; Paxson, A. T.; Varanasi, K. K.; Patankar, N. A. *Phys. Rev. Lett.* **2011**, *106*, 036102.
(32) Ozisik, M. N. *Heat Conduction*, 2nd ed.; Wiley-Interscience: New York, 1993.
(33) Duvivier, D.; Seveno, D.; Rioboo, R.; Blake, T. D.; De Coninck, J. *Langmuir* **2011**, *27* (21), 13015−13021.
(34) Bartolo, D.; Bouamrirene, F.; Verneuil, E.; Buguin, A.; Silberzan, P.; Moulinet, S. *Europhys. Lett.* **2006**, *74* (2), 299−305.
(35) Haller, K. K.; Poulikakos, D.; Ventikos, Y.; Monkewitz, P. *J. Fluid Mech.* **2003**, *490*, 1−14.
(36) Field, J. E.; Camus, J. J.; Tinguely, M.; Obreschkow, D.; Farhat, M. *Wear* **2012**, *290*, 154−160.
(37) Field, J. E. *Phys. Med. Biol.* **1991**, *36* (11), 1475−1484.
(38) Sikalo, S.; Marengo, M.; Tropea, C.; Ganic, E. N. *Exp. Therm Fluid Sci.* **2002**, *25* (7), 503−510.
(39) Eddi, A.; Winkels, K. G.; Snoeijer, J. H. *Phys. Fluids* **2013**, *25*, 013102.
(40) Mani, M.; Mandre, S.; Brenner, M. P. *J. Fluid Mech.* **2010**, *647*, 163−185.
(41) Hicks, P. D.; Purvis, R. *J. Fluid Mech.* **2010**, *649*, 135−163.
(42) Vincent, F.; Le Goff, A.; Lagubeau, G.; Quere, D. *J. Adhes.* **2007**, *83* (10), 897−906.
(43) Mandre, S.; Mani, M.; Brenner, M. P. *Phys. Rev. Lett.* **2009**, *102*, 13.
(44) Park, J. G.; Lee, S. H.; Ryu, J. S.; Hong, Y. K.; Kim, T. G.; Busnaina, A. A. *J. Electrochem. Soc.* **2006**, *153* (9), G811−G814.
(45) Allen, D. M.; Jefferies, P. *CIRP Ann.* **2006**, *55*, 4.
(46) Kannarpady, G. K.; Khedir, K. R.; Ishihara, H.; Woo, J.; Shin, O. D.; Trigwell, S.; Ryerson, C.; Biris, A. S. *ACS Appl. Mater. Inter.* **2011**, *3* (7), 2332−2340.
(47) Verho, T.; Bower, C.; Andrew, P.; Franssila, S.; Ikkala, O.; Ras, R. H. A. *Adv. Mater.* **2011**, *23* (5), 673−678.